



Human influence on climate detectable in the late 19th century

Benjamin D. Santer^{a,b,1} , Susan Solomon^c , David W. J. Thompson^{d,e}, Qiang Fu^f , and Yaowei Li^c

Affiliations are included on p. 11.

Edited by Ralph F. Keeling, Scripps Institution of Oceanography, La Jolla, CA; received January 13, 2025; accepted April 22, 2025, by Editorial Board Member Mark H. Thiemens

The physics of the heat-trapping properties of CO₂ were established in the mid-19th century, as fossil fuel burning rapidly increased atmospheric CO₂ levels. To date, however, research has not probed when climate change could have been detected if scientists in the 19th century had the current models and observing network. We consider this question in a thought experiment with state-of-the-art climate models. We assume that the capability to make accurate measurements of atmospheric temperature changes existed in 1860, and then apply a standard “fingerprint” method to determine the time at which a human-caused climate change signal was first detectable. Pronounced cooling of the mid- to upper stratosphere, mainly driven by anthropogenic increases in carbon dioxide, would have been identifiable with high confidence by approximately 1885, before the advent of gas-powered cars. These results arise from the favorable signal-to-noise characteristics of the mid- to upper stratosphere, where the signal of human-caused cooling is large and the pattern of this cooling differs markedly from patterns of intrinsic variability. Even if our monitoring capability in 1860 had not been global, and high-quality stratospheric temperature measurements existed for Northern Hemisphere mid-latitudes only, it still would have been feasible to detect human-caused stratospheric cooling by 1894, only 34 y after the assumed start of climate monitoring. Our study provides strong evidence that a discernible human influence on atmospheric temperature has likely existed for over 130 y.

climate change detection and attribution | stratospheric temperature | satellite temperature data

In the late 1850s and early 1860s, Eunice Foote and John Tyndall made seminal experimental discoveries about the heat-trapping properties of CO₂ and other greenhouse gases (1). Their work, along with earlier insights from Fourier, Pouillet, and de Saussure, paved the way for subsequent climate modeling efforts by the Swedish chemist Svante Arrhenius (2). Arrhenius recognized that human-caused fossil fuel burning contributed to increases in CO₂ and estimated that surface temperature could increase by 4 °C in response to a doubling of atmospheric CO₂ levels (3).

In tandem with this developing understanding of the greenhouse effect in the mid- to late 1800s, the data required for efforts to identify human fingerprints on climate were accumulating. At Earth’s surface, observers at many urban locations in Europe and North America started systematic daily measurements of surface temperature in the 1860s (4). The first use of unpiloted weather balloons to study the free atmosphere was in 1892, when the French physicist Gustave Hermite and journalist Georges Besançon launched balloons carrying a device for measuring temperature and pressure (5).

The pioneering work of Hermite and Besançon was followed at the end of the 1800s by more systematic balloon-based measurements of atmospheric temperature conducted by Léon Teisserenc de Bort in France (6, 7) and Richard Assmann in Germany (8). Using balloons made of paper, silk, and rubber, Teisserenc de Bort and Assmann demonstrated that temperature did not simply continue to decrease with increasing height above Earth’s surface. They found that above roughly 11 to 14 km, there was a layer in which temperature was uniform or increased with height. This marked the discovery of the stratosphere.

The pioneering work of Teisserenc de Bort and Assmann led to efforts to construct radiosonde-based estimates of global-scale changes in tropospheric and lower stratospheric temperature. Unlike the first weather balloons, radiosondes transmitted temperature measurements to ground stations via radio. A summary of the history of radiosonde measurements (9) argues that the International Geophysical Year in 1958 marked the beginning of true global records of the temperature of the free atmosphere. Other analysts report global-scale monitoring of upper-air temperature dating back to 1946 (10). Statistical reconstructions of global atmospheric temperature changes

Significance

When could scientists have first known that fossil fuel burning was significantly altering global climate? We attempt to answer this question by performing a thought experiment with model simulations of historical climate change. We assume that the capability to monitor global-scale changes in atmospheric temperature existed as early as 1860 and that the instruments available in this hypothetical world had the same accuracy as today’s satellite-borne microwave radiometers. We then apply a pattern-based “fingerprint” method to disentangle human and natural effects on climate. A human-caused stratospheric cooling signal would have been identifiable by approximately 1885, before the advent of gas-powered cars. Our results suggest that a discernible human influence on atmospheric temperature has likely existed for over 130 y.

Author contributions: B.D.S., S.S., D.W.J.T., and Q.F. designed research; B.D.S. performed research; B.D.S., S.S., D.W.J.T., and Q.F. analyzed data; and B.D.S., S.S., D.W.J.T., Q.F., and Y.L. wrote the paper.

The authors declare no competing interest.

This article is a PNAS Direct Submission. R.F.K. is a guest editor invited by the Editorial Board.

Copyright © 2025 the Author(s). Published by PNAS. This open access article is distributed under [Creative Commons Attribution-NonCommercial-NoDerivatives License 4.0 \(CC BY-NC-ND\)](https://creativecommons.org/licenses/by-nc-nd/4.0/).

¹To whom correspondence may be addressed. Email: bensanter1289@gmail.com.

This article contains supporting information online at <https://www.pnas.org/lookup/suppl/doi:10.1073/pnas.2500829122/-DCSupplemental>.

Published June 16, 2025.

constrained by “historical upper-air data and surface data” are available from as early as 1918 onward (11).

As scientists began to measure atmospheric temperature, large ice sheets in Antarctica and Greenland were preserving a signal of changes in atmospheric CO₂, methane, and other greenhouse gases (12, 13). This signal arose from the ramping up of fossil fuel burning during the Industrial Revolution. The ice cores revealed that carbon dioxide was growing at a rate of roughly 2.5 ppmv per decade over 1860 to 1899 (*SI Appendix*, Fig. S1).*

In the late 1800s and early 1900s, therefore, there was emerging scientific understanding that fossil fuel burning produced CO₂, thus enhancing Earth’s natural greenhouse effect, and that this enhancement would warm Earth’s surface. The capability to measure changes in the temperature of the free atmosphere was developing rapidly. However, there was not yet an understanding of how elevated levels of CO₂ might change the vertical structure of atmospheric temperature in the stratosphere and troposphere. This understanding became available with publication of the modeling work of Manabe and Wetherald in the 1960s (15).

Few studies have considered when the human influence on climate predicted by Foote, Tyndall, Arrhenius, and others might first have been detectable. Prior work in the detection of early anthropogenic signals has focused on paleoclimatic reconstructions and/or long-term observations of changes in surface temperature from spatially limited samples (16, 17). None of these previous investigations examined global changes in the temperature of the troposphere, where temperature fluctuations arising from intrinsic variability are spatially less noisy than at the surface, thus facilitating early detection of anthropogenic effects. Nor has previous work explored the possibility of early detection of an anthropogenic signal in the stratosphere, a region with a large expected anthropogenic signal and distinct differences between this signal pattern and patterns of intrinsic variability (18).

Here we pose a simple question: when could scientists have first known that fossil fuel burning was significantly altering global climate? We attempt to answer this question by performing a thought experiment with climate model simulations of historical changes in atmospheric temperature. We assume that: 1) the capability to monitor global changes in atmospheric temperature existed as early as 1860; 2) instruments available at that time had the same accuracy as today’s satellite microwave radiometers; and 3) the model simulations of historical climate change that are analyzed in our thought experiment use reliable estimates of CO₂ changes from ice cores and direct air measurements (19).

In this hypothetical “Gedanken world,” when could scientists have first detected a human fingerprint on climate relative to the natural variability of the climate system? We also ask a related question: when could human effects on climate have been identified if accurate measurement of atmospheric temperature after 1860 was not possible globally, but only for a limited geographical region, such as mid-latitudes of the Northern Hemisphere? The latter region is where the first measurements of stratospheric temperature were made, and has the advantage of avoiding polar regions characterized by large stratospheric temperature variability (20).

Our thought experiment has multiple goals. The first is to estimate the detection time of human-caused temperature fingerprints for different layers of Earth’s atmosphere and different geographical regions. The second is to understand how detection time varies based on different choices of the assumed “start date”

for climate monitoring. We examine a set of eight start dates. The first is in 1860, near the beginning of the rapid anthropogenic increase in fossil fuel burning. The final start date is in 1986, when a globally complete satellite record of tropospheric and stratospheric temperature change commenced and signal detection could be performed in the real world (21, 22).

The choice of the assumed monitoring start date influences not only the size of the human-caused climate signal that is sampled, but also the sampling of naturally forced climate variability caused by large volcanic eruptions and fluctuations in solar irradiance (23, 24). The stratospheric volcanic aerosol from large eruptions scatters some portion of incoming solar radiation back to space, thus cooling the troposphere, while simultaneously warming the stratosphere by absorbing solar radiation and outgoing long-wave radiation (25). Changes in total solar irradiance (TSI) occur on timescales ranging from roughly 11 y to centuries, causing coherent warming of the stratosphere in high TSI periods and coherent stratospheric cooling in low TSI periods (26). Our set of start dates allows us to compare detection of human fingerprints in periods with reduced and pronounced volcanic and solar activity, thus yielding insights into the impact of both forcings on fingerprint detection times.

As we will show, our thought experiment suggests that human influence on atmospheric temperature could have been identified with high confidence in the late 1800s, at a time when the decadal increase in atmospheric CO₂ was roughly a factor of nine smaller than in the first 25 y of the 21st century. This finding indicates that significant human interference with Earth’s climate is not a new phenomenon. It has existed for over 130 y.

Global-Mean Changes

We analyze model simulations of historical climate change, projected future changes in climate, and natural internal variability. The historical simulations end in 2014 and were extended with results from future change projections. We refer to these extended simulations as HIST_{ext} runs. For the 1986 monitoring start date, extension facilitates comparisons of anthropogenic fingerprint detection times in the HIST_{ext} realizations and in the actual satellite temperature data (21, 22, 31) over the full 39-y period from 1986 to 2024.

All simulations were performed under phase 6 of the Coupled Model Intercomparison Project (CMIP6) (32). We examine a total of 32 different realizations of historical climate change from nine different CMIP6 models. Our focus is on layer-average temperatures for the troposphere and the stratosphere. In observations, these temperatures are obtained with satellite-based microwave sounders, including the Stratospheric Sounding Unit (SSU) and the Microwave and Advanced Microwave Sounding Units (MSU and AMSU) (21, 22). To conduct our thought experiment, we calculate synthetic satellite temperatures from all model simulations (18). Further details of all datasets and processing are available in the *Materials and Methods* and *SI Appendix*.

Fig. 1 shows time series of global-mean monthly mean atmospheric temperature change over 1860 to 2024 for six atmospheric layers: channels 3, 2, and 1 of the Stratospheric Sounding Unit (SSU3, SSU2, and SSU1), lower stratospheric temperature from the Microwave and Advanced Microwave Sounding Units (TLS), MSU/AMSU total tropospheric temperature (TTT), and MSU/AMSU lower tropospheric temperature (TLT). These six layers span an altitude range extending from the surface to approximately 45 km above Earth’s surface.

* Ice cores also recorded even earlier changes in CO₂ and CH₄, dating back nearly 5,000 to 7,000 y before the Industrial Revolution. The “Early Anthropogenic Hypothesis” posits that these changes in atmospheric composition may have been the result of deforestation and early agricultural practices (14).

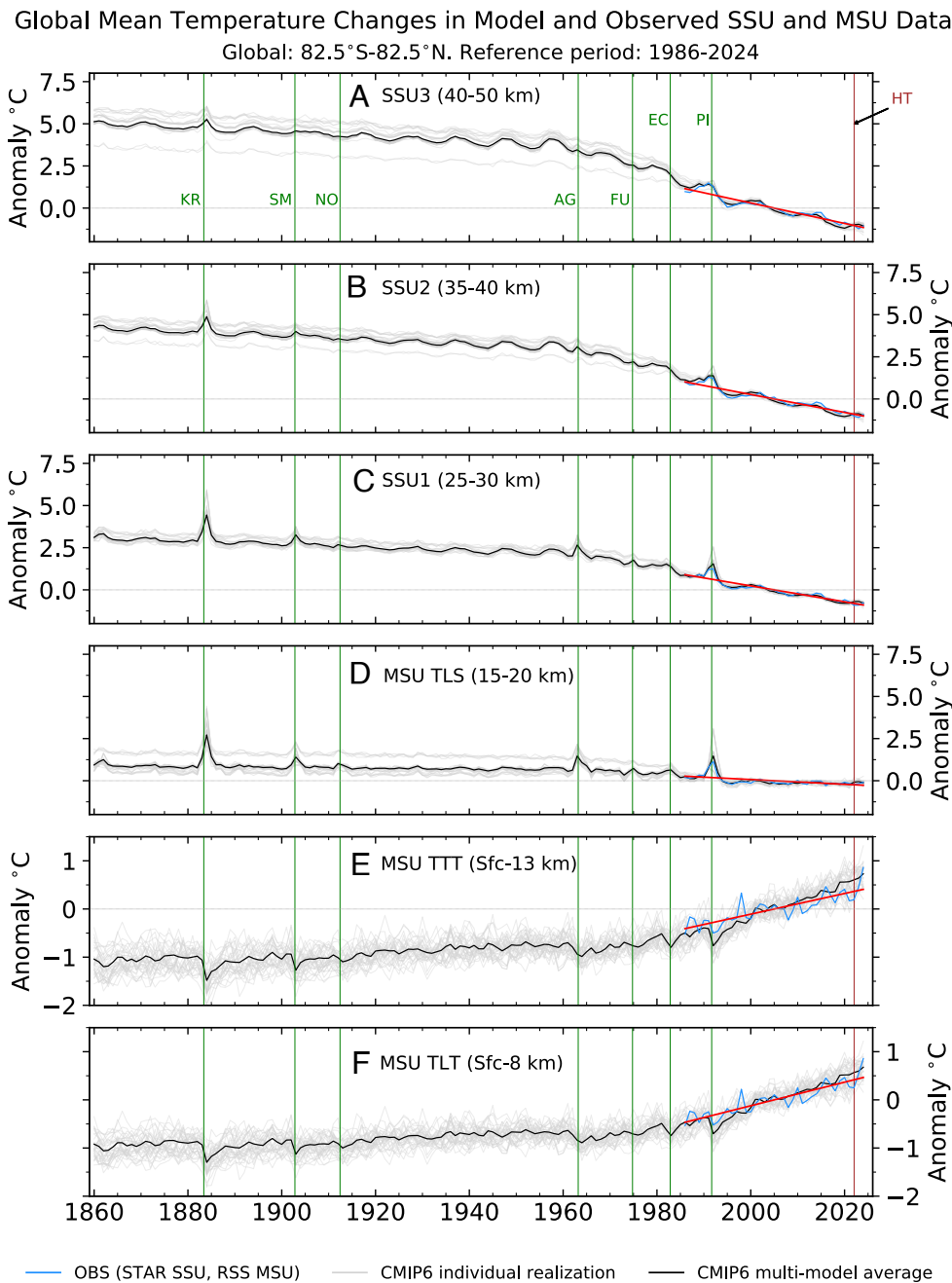


Fig. 1. Observed and simulated changes in global-mean annual-mean temperature in six atmospheric layers. Results are synthetic and observed temperatures averaged over the layers sampled by the primary satellite instruments used to measure atmospheric temperatures: the SSU (panels A–C) (21) and the MSU/AMSU. MSU/AMSU provides lower stratospheric temperature (TLS), total tropospheric temperature (TTT), and lower tropospheric temperature (TLT) (panels D–F), respectively (22). Approximate altitude ranges of the weighting functions for these layers are given in brackets (27, 28). Results are anomalies relative to climatological means over 1986 to 2024. Model simulations are for the period 1860 to 2024 and are from nine different CMIP6 models and 32 realizations of historical climate change (see Materials and Methods and *SI Appendix*). Vertical green lines are the start dates of major volcanic eruptions: KR = Krakatoa; SM = Santa María; NO = Novarupta; AG = Agung; FU = Fuego; EC = El Chichón; PI = Pinatubo. The vertical brown line marked HT denotes the unusual Hunga Tonga eruption. Unlike the other eruptions shown in the figure, Hunga Tonga injected a large amount of water vapor into the stratosphere and mesosphere (29). Forcing by “small” early 21st century eruptions was included (up until December 2014) in the CMIP6 historical runs, but the start dates of these eruptions are not shown here (30). The red lines are least-squares linear trends in the satellite temperature data.

In both the HIST_{ext} simulations and the satellite data, the SSU layers exhibit pronounced stratospheric cooling (18, 33). Cooling arises from the direct radiative response to: 1) anthropogenic emissions of CO₂ and other well-mixed greenhouse gases, which increase the longwave emissivity of the stratosphere; and 2) anthropogenically driven ozone losses, which decrease the amount of shortwave radiation absorbed in the stratosphere (15, 27, 34–39). As predicted in 1967 (15), CO₂-induced stratospheric

cooling amplifies higher in the stratosphere (18, 40, 41). For SSU3, SSU2, SSU1, and TLS, the CMIP6 multimodel average global-mean stratospheric cooling over 1860 to 2024 is −6.0, −5.0, −3.7, and −1.1 °C, respectively.

In the HIST_{ext} runs, long-term stratospheric cooling in the SSU layers is small and linear from 1860 until roughly 1960, increasing markedly thereafter. The roughly 11-y cycle in TSI is particularly prominent in SSU3 and SSU2, along with longer-

timescale temperature variations associated with changes in the amplitude of the 11-y cycle (26). In all four stratospheric layers, short-term (1 to 3 y) warming signals occur after large explosive volcanic eruptions (25, 38). These signals are generally largest in the lower stratosphere[†] where most volcanic aerosol resides.

The two tropospheric layers warm in both the satellite data and the model simulations. The CMIP6 multimodel average tropospheric warming over 1860 to 2024 is roughly 1.3 and 1.2 °C for TTT and TLT (respectively). The simulated warming rate is small and linear from 1860 until approximately 1980, increasing thereafter. This increase in warming rate is partly due to the introduction of widespread controls on anthropogenic sulfur emissions in the late 1970s, which damped sulfate aerosol-induced tropospheric cooling (42). Superimposed on long-term tropospheric warming are the short-term (3- to 5-y) tropospheric cooling signals of major volcanic eruptions (25, 43). Due to the large thermal inertia of the ocean, volcanic temperature signals persist longer in the troposphere than in the stratosphere (44).

Fingerprinting and Signal-to-Noise Ratios

Fingerprinting is used to separate human and natural effects on climate (45–50). Here, we apply a standard fingerprint method (18) to determine whether (and when) model-predicted patterns of the combined response to anthropogenic and natural external forcing are identifiable in each of the 32 individual CMIP6 HIST_{ext} realizations. The fingerprint patterns that we search for are dominated by the large anthropogenically driven stratospheric cooling and tropospheric warming shown in Fig. 1 and in *SI Appendix*, Fig. S2 (18). There are different fingerprints for each analysis period, geographical domain, and set of atmospheric layers. Each fingerprint is the leading empirical orthogonal function (EOF) of zonal-mean temperature changes in the multimodel average of the CMIP6 HIST_{ext} runs (*Materials and Methods* and *SI Appendix*).

We explore fingerprint detectability for assumed monitoring start dates of 1860, 1900, 1920, 1940, 1950, 1960, 1970, and 1986. We determine whether the CMIP6 multimodel average fingerprints for different vertical and geographical domains would have been identifiable within a 40-y temperature monitoring window after the start date. This window length was chosen because it is similar to the actual 39-y length of the gap-free SSU and MSU/AMSU satellite temperature records (18). Fingerprint detection times are based on signal-to-noise (S/N) ratios. These ratios vary as a function of timescale L , with L ranging from 5 to 40 y in increments of 1 y. The earliest possible fingerprint detection time, therefore, is 5 y after the start date (e.g., in 1990 for a 1986 start date).

We perform fingerprinting for four vertical domains and four geographical domains, so there are 16 different sets of timescale-dependent S/N ratios for a given monitoring start date. The vertical domains are the six layers in Fig. 1, the three SSU layers, the three MSU layers (TLS, TTT, and TLT), and the two tropospheric layers (TTT and TLT). We refer to these domains subsequently as SSU+MSU, SSU, MSU, and TROP, respectively. The geographical domains are 90°S–90°N, 0°–90°N, 90°S–0°, and 40°N–55°N.

Fig. 2 shows the fingerprint pattern $F(x)$ for the four vertical domains and for three selected start dates: 1860, 1920, and 1986. Fingerprints for the 1860 and 1986 start dates were

calculated over analysis periods that exclude the effects of the 1883 Krakatoa eruption and that reduce the influence of the 1991 Pinatubo eruption—i.e., over 1860 to 1882 and over 1994 to 2024 (respectively).

In all three of the analysis periods in Fig. 2, the SSU+MSU and MSU $F(x)$ patterns are characterized by latitudinally coherent tropospheric warming and stratospheric cooling. This is the expected response to human-caused CO₂ increases (15, 27, 34, 36, 38, 39, 51). As the fingerprint calculation period advances from 1860 to 1920 to 1994, anthropogenic greenhouse-gas forcing increases and the size of stratospheric cooling and tropospheric warming increases. Stratospheric cooling amplifies with increasing height in all three analysis periods, although only weakly over the analysis period that starts in 1860 (Fig. 2 A–F) (15, 18).

In the lower S/N environment of the troposphere (18), only the most recent 1994–2024 analysis period with the largest net anthropogenic forcing displays the predicted anthropogenic signals (52) of hemispherically asymmetric warming and polar amplification of warming in the NH (Fig. 2 I and L). The TROP fingerprint patterns in the earlier 1860–1882 and 1920–1959 analysis periods primarily reflect ENSO-induced temperature variability in the tropical troposphere (Fig. 2 J and K). This may be partly due to the relatively small ensemble sizes of HIST_{ext} realizations in the nine models examined here (*SI Appendix*, Table S1). As a result, the multimodel average (MMA) used to estimate EOFs retains a larger imprint of internal variability in the earlier analysis periods when external forcing is still weak (see MMA results in Fig. 1 E and F).

Fig. 3 shows signals and S/N ratios for four selected monitoring start dates: 1860, 1900, 1920, and 1986. Results are for the global geographical domain and for each of the four vertical domains. The time-evolving signals provide information about the spatial similarity between the CMIP6 multimodel average fingerprints and the 32 individual CMIP6 extended historical realizations (see Fig. 3 caption, *Materials and Methods*, and *SI Appendix*).

If temperature changes in the individual HIST_{ext} realizations are becoming more similar to the searched-for fingerprints, there will be a positive trend in the pattern similarity statistic. If this trend is significantly larger than trends in pattern similarity between the fingerprints and internal variability, the S/N ratios will exceed a stipulated significance level (1% here) at some value L_d of the trend length L . For calculation of a valid detection time, we require that S/N remains above the stipulated significance level for all L values greater than L_d and less than or equal to L_{max} years (18).[‡] The denominator of the S/N ratios is calculated with output from CMIP6 control runs, which provide estimates of the “noise” of natural internal variability. The adequacy of these noise estimates is considered later.

Consider first the 1860 results (Fig. 3 A and B). For the vertical domains that incorporate information from the mid- to upper stratosphere (SSU+MSU and SSU), the signals for analysis periods ending between roughly 1865 and 1867 are positive. For these initial periods, small, CO₂-induced stratospheric cooling is already occurring, and is in phase with natural cooling of the stratosphere caused by the transition to solar minimum in ca. 1867.[§] As solar forcing transitions to the next solar maximum in roughly 1872, the signal strength for the SSU+MSU and SSU domains begins to decline. This decline reflects an increase in TSI, which warms the stratosphere and partially offsets CO₂-driven stratospheric cooling.

[†]One exception is the eruption of Hunga Tonga in January 2022, which injected a large amount of water vapor into the stratosphere and mesosphere, cooling both layers for several years after the eruption (29).

[‡]Other less restrictive definitions of detection time could yield earlier fingerprint detection.

[§]See figure 1 in ref. 26.

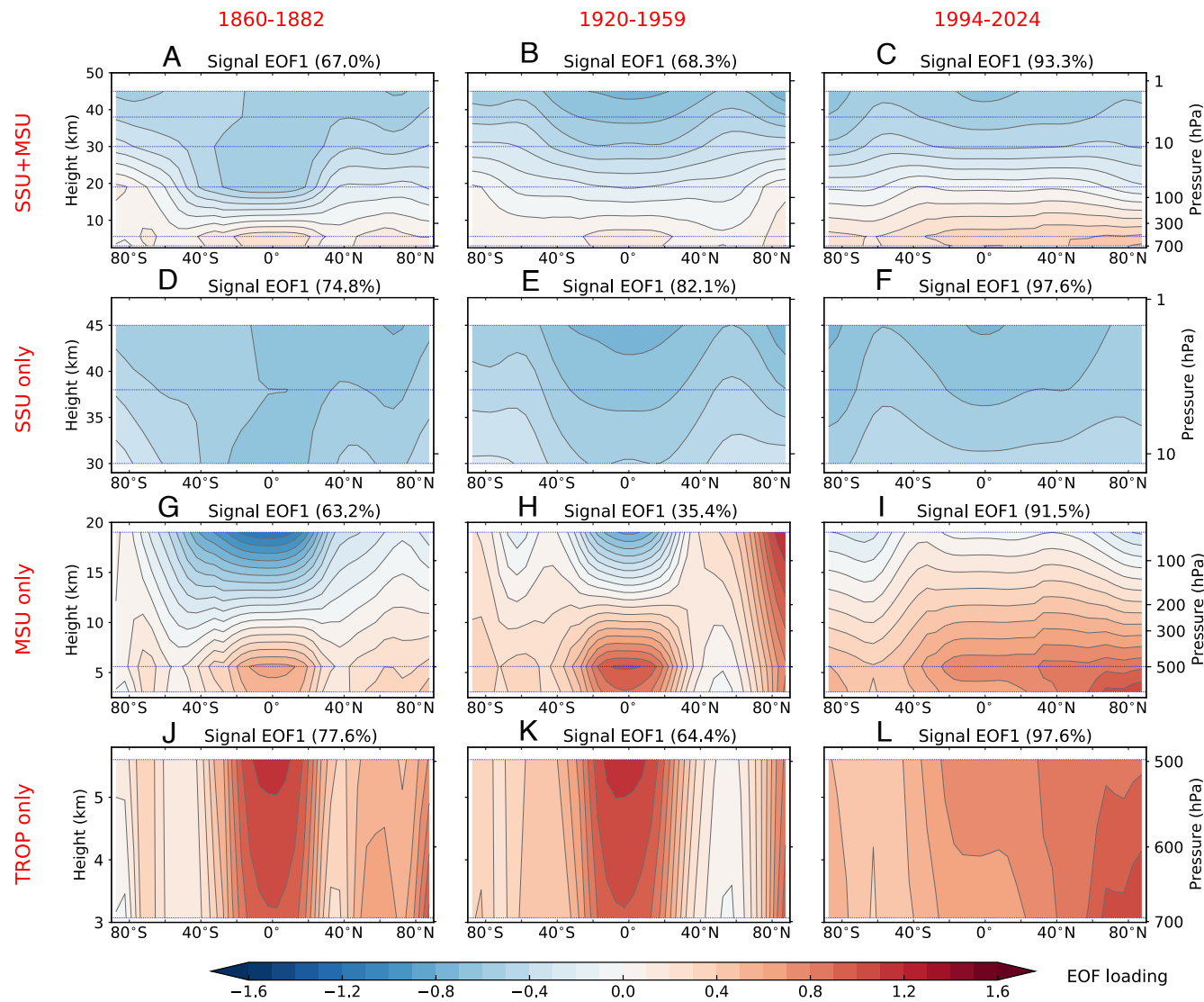


Fig. 2. Model fingerprints of atmospheric temperature change in response to combined anthropogenic and natural external forcing. Fingerprints were calculated for four vertical domains: SSU+MSU (panels A, B, and C), SSU (panels D, E, and F), MSU (panels G, H, and I), and TROP (panels J, K, and L). Results are for three different periods: 1860–1882 (panels A, D, G, and J), 1920–1959 (panels B, E, H, and K), and 1994–2024 (panels C, F, I, and L). Each fingerprint pattern, $F(x)$, is the first EOF of the CMIP6 multimodel average zonal-mean annual-mean atmospheric temperature changes (see Materials and Methods and SI Appendix). The choice of the 1860–1882 and 1994–2024 periods reduces the influence of the large Krakatoa and Pinatubo eruptions (which occurred in 1883 and 1991, respectively). The period 1920–1959 has few major eruptions (Fig. 1). All results are for global geographical coverage. The variance explained by each EOF is given in brackets. EOF loadings are plotted at the approximate heights of the maxima of each SSU and MSU weighting function, indicated by dotted horizontal blue lines. Results were smoothly interpolated in the vertical.

For analysis periods ending shortly after the eruption of Krakatoa in 1883, signal trends decrease markedly and change sign from positive to negative. This sign change occurs because Krakatoa warmed the stratosphere and cooled the troposphere (Fig. 1), the converse of the CO₂ signal. As a result of the Krakatoa eruption, S/N ratios for most HIST_{ext} realizations dip below the 1% significance level for analysis periods ending between 1883 and 1885 (Fig. 3B). This holds for all four vertical domains. In the SSU+MSU and SSU domains, S/N ratios for most HIST_{ext} realizations recover for periods ending after 1885, increasing above the 1% significance level and remaining above the 1% level for values of $L >$ roughly 25 to 30 y.

Similar influences of natural external forcing are evident for the other three start dates in Fig. 3. For a 1900 start date, signal trends ending between approximately 1904 and 1908 are negative because of an increase in TSI in the transition to a solar maximum with a broad, complex peak in the 1904–1908 time period (26).

In contrast, a 1920 start date yields positive SSU+MSU and SSU signal trends for the initial analysis periods, as TSI decreases toward solar minimum in the mid-1920s (26), in phase with anthropogenic stratospheric cooling. In general, as the analysis period L increases, CO₂-induced stratospheric cooling becomes larger relative to solar-driven stratospheric temperature changes, so the impact of solar forcing on signal trends and S/N ratios diminishes. We note, however, that the 1920 start date samples larger low-frequency variations in the amplitude of the 11-y solar cycle (26) (Fig. 1). This yields “ripples” with a roughly 11-y periodicity in signals and S/N ratios (Fig. 3E and F).

As in the case of Krakatoa, the eruption of Mt. Pinatubo in 1991 has a pronounced effect on atmospheric temperature (Fig. 1). For a 1986 start date, Pinatubo’s large stratospheric warming and tropospheric cooling strongly influences the first 5- to 7-y analysis periods, leading to negative 5- to 7-y signal trends (Fig. 3G). In the recovery from Pinatubo, the volcanically

Sensitivity of Signal and S/N Ratio to Assumed Monitoring Start Date

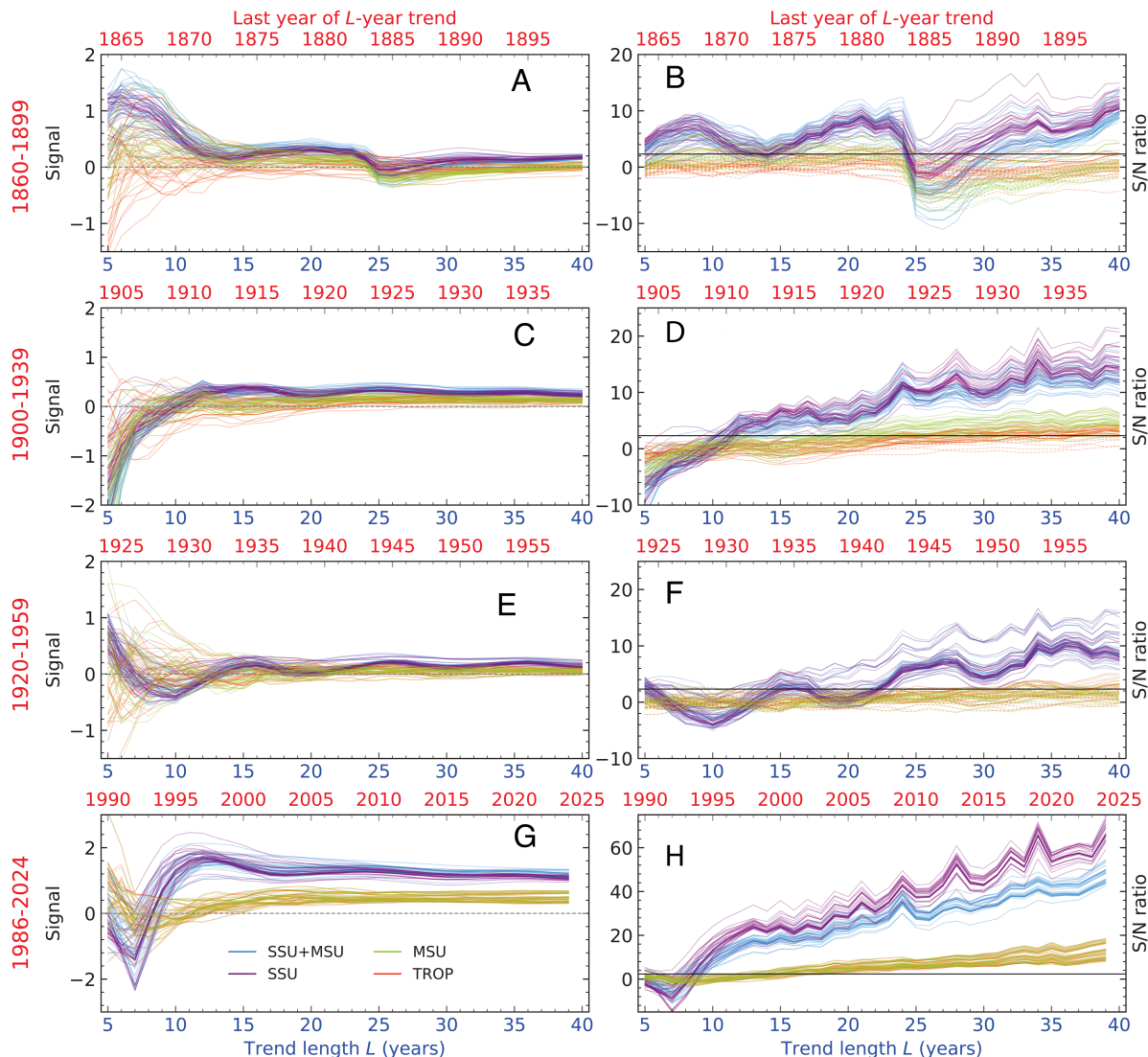


Fig. 3. Influence of the “start date” for detecting human-caused atmospheric temperature signals on signals and S/N ratios. Results are for global geographical coverage and four vertical domains (SSU+MSU, SSU, MSU, and TROP). The four rows correspond to monitoring start dates of 1860 (panels A, B), 1900 (panels C, D), 1920 (panels E, F), and 1986 (panels G, H). The signals (left column) were calculated by projecting latitude-height temperature data from 32 individual CMIP6 HIST_{ext} realizations onto the fingerprint $F(x)$ (Fig. 2). Trends of increasing length L years were computed from the resulting projection time series. CMIP6 control run temperature data were then projected onto $F(x)$, yielding the projection time series $N_{ctt}(t)$. The noise $\sigma_{ctt}(L)$ is estimated by fitting nonoverlapping L -year trends to $N_{ctt}(t)$ and calculating the SD of the L -year trend distribution. The S/N ratio (right column) is the L -year signal trend divided by the respective values of $\sigma_{ctt}(L)$. For each start date, L varies from 5, 6, … L_{\max} years, with $L_{\max} = 39$ years for 1986 and 40 years for all other start dates. The horizontal black line in panels B, D, F, and H is the 1% significance level.

forced temperature changes are in phase with CO₂-induced stratospheric cooling and tropospheric warming, leading to large increases in signal trend size for trends ending between 1993 and 1996.

One general feature of Fig. 3 is that for all four vertical domains, S/N ratios for the longest analysis timescales tend to increase as the monitoring start date advances (note the differences in y-axis ranges in Fig. 3 B, D, F, and H). This increase in S/N with later start dates primarily reflects the increased anthropogenic forcing over time. Another general feature is that S/N ratios for 40-y analysis timescales are invariably larger for the SSU+MSU and SSU domains than in MSU and TROP. This systematic difference is attributable to larger signals in the stratosphere, as well as to greater orthogonality

between stratospheric fingerprint and noise patterns (18). The SSU+MSU and SSU $F(x)$ patterns are therefore more effective at filtering out natural variability noise than the MSU or TROP patterns.

Fingerprint Detection Times

Values of the detection time t_d were calculated using the S/N ratios in Fig. 3. Recall from the previous section that t_d is the last year of the L -year signal trend at which the S/N ratio rises above the 1% significance level and then remains above the 1% level for all longer trend lengths.

Consider first the results for an 1860 monitoring start date and global geographical coverage. The model-predicted SSU and

SSU+MSU fingerprints (which as noted above are dominated by anthropogenic forcing) are identifiable in all 32 HIST_{ext} realizations. For the SSU domain, a human fingerprint on mid- to upper stratospheric temperature would have been detectable not only for global measurements (by 1885 on average) but also for the limited NH mid-latitude region (by 1894 on average). Across the four different geographical regions, the average fingerprint detection time for the SSU+MSU layers occurs roughly 2 to 4 y later relative to the SSU domain. This delay arises because the SSU+MSU layers include tropospheric levels with lower S/N characteristics (18). The MSU and TROP vertical domains are dominated by the tropospheric levels with smaller signals and greater similarity between signal and noise patterns, thus yielding fingerprint detection before 1900 in only a limited number of HIST_{ext} realizations.

As the start date for monitoring advances and the 40-y windows used for fingerprinting sample larger anthropogenic signals, the number of years required for fingerprint identification does not decrease monotonically. For the SSU vertical domain and global geographical coverage, the average time required for fingerprint detection after the 1860, 1900, 1920, and 1986 start dates is 27, 10, 20, and 8 y (respectively; Fig. 4). The increase in required time between the 1900 and 1920 start dates is due to the larger amplitude of the 11-y solar cycle sampled by the 1920 start date (Fig. 1) (26). As noted above, large-amplitude TSI changes yield periods when solar forcing reinforces or partly offsets CO₂-induced stratospheric cooling, causing noticeable 11-y ripples in signal strength and in S/N ratios (Fig. 3 E and F). One of these ripples occurs for analysis periods that end near a solar maximum in the late 1930s, causing S/N ratios in many HIST_{ext} realizations to temporarily dip below the 1% significance threshold, thus delaying fingerprint detection (Fig. 3F).

For the 1986 start date, the model-predicted fingerprints for all four vertical domains and all four geographical regions are identifiable with high confidence in each of the 32 HIST_{ext} realizations. This is a striking result. The large stratospheric warming and tropospheric cooling signals caused by Pinatubo in 1991 hamper detection of CO₂-induced stratospheric cooling and tropospheric warming. Yet despite the countervailing effect of Pinatubo, ubiquitous detection of an anthropogenic fingerprint in the HIST_{ext} runs occurs, on average, as early as 1993 for SSU with global coverage, and t_d is no later than 2002 for TROP with Southern Hemisphere coverage.

In most cases, the t_d values in actual satellite data are within the model ranges of t_d values across the 32 members of the CMIP6 multimodel ensemble. The exceptions are the MSU and TROP results for the SH and the 40°N–55°N domains. For UAH and STAR, the t_d values in these two vertical domains and geographical regions are outside the range of model results. This is because both UAH and STAR have smaller tropospheric warming over 1986 to 2024 than RSS or most CMIP6 models (18).

Signals and S/N ratios for four additional start dates (1940, 1950, 1960, and 1970) are shown in *SI Appendix*, Fig. S3, along with the t_d values calculated from the S/N ratios (*SI Appendix*, Fig. S4). In contrast to the t_d results for the 1900 and 1920 start date cases in Fig. 4, the length of monitoring period required for fingerprint detection in *SI Appendix*, Fig. S4 decreases monotonically as the start date advances. This holds for all four vertical and horizontal domains. The reason for this result is that after 1940, anthropogenic signals of stratospheric cooling and tropospheric warming are sufficiently large to overwhelm the combined noise of intrinsic variability and solar and volcanic forcing—which was not the case for a 1920 start date. After 1940,

therefore, as the start date advances and larger anthropogenic signals are sampled, S/N increases and fingerprint detection requires a shorter length of analysis period.

Results for the 1960 monitoring start date sample the effects of three major eruptions: Agung, El Chichón, and Pinatubo in 1963, 1982, and 1991, respectively (Fig. 1). In spite of the large tropospheric cooling signals caused by these eruptions, the model-predicted TROP fingerprints are robustly identifiable in the CMIP6 HIST_{ext} realizations. This holds for all four geographical regions (see third panel of *SI Appendix*, Fig. S4). For TROP, the average detection times across the 32-member ensemble range from roughly 1984 for the Southern Hemisphere to 1992 for the 40°N–55°N latitude band. The post-1960 anthropogenic forcing, therefore, is sufficiently large to overwhelm the volcanically induced tropospheric cooling.

Simulated and Observed Temperature Variability

How reliable are these detection times? The answer to this question depends on the credibility of CMIP6 internal variability estimates. Systematic model underestimates of decadal internal variability—the average detection timescales for many combinations of vertical domain and geographical region in Fig. 4 and *SI Appendix*, Fig. S4—would bias our results toward positive identification of anthropogenic fingerprints and earlier detection times. Other studies with CMIP5 and CMIP6 models suggest that systematic low biases in decadal variability are not a concern for tropospheric temperature (53, 54). Few such comparisons exist for stratospheric temperature (55).

Here we compare observed atmospheric temperature variability with model results from unforced preindustrial control runs and forced HIST_{ext} simulations. Control runs provide estimates of $T_{ctl}(t)$, the “pure” internal variability of atmospheric temperature. In contrast, subtraction of the multimodel average temperature time series from each individual HIST_{ext} realization yields both pure internal variability and intermodel differences in the response to external forcings. The latter can be appreciable, as in the case of the simulated temperature response to Pinatubo in TLS and SSU1, the layers with the largest loadings of the volcanic aerosol from Pinatubo (*SI Appendix*, Figs. S5 and S6). We refer to the “MMA-removed” residual variability in the HIST_{ext} runs as $T_{hist}(t)$.

In the real world, there is only one realization of the combined effects of intrinsic variability and the response to external forcing. This introduces uncertainty in separating $T_{obs}(t)$, the observed intrinsic variability, from the forced response. We estimate $T_{obs}(t)$ here by applying a standard regression method (54, 56, 57) to remove forced temperature signals from observations (*SI Appendix*, Figs. S5 and S6). Our signals are the CMIP6 global-mean monthly mean MMA time series over 1986 to 2024 in the six atmospheric layers of interest.

Values of $T_{obs}(t)$ contain contributions from three sources: 1) pure internal variability; 2) differences between the real-world response to external forcing and the model-average forced response; and 3) forcings that affected observed atmospheric temperature but were not included in the HIST_{ext} runs, such as the January 2022 Hunga Tonga eruption (29). The CMIP6 HIST_{ext} simulations analyzed here were performed before this event occurred.

Given the relatively short observational record length (39 y), the longest timescale on which we can make useful comparisons of modeled and observed internal variability is roughly 10 y. We focus on this timescale by digitally filtering $T_{ctl}(t)$, $T_{hist}(t)$,

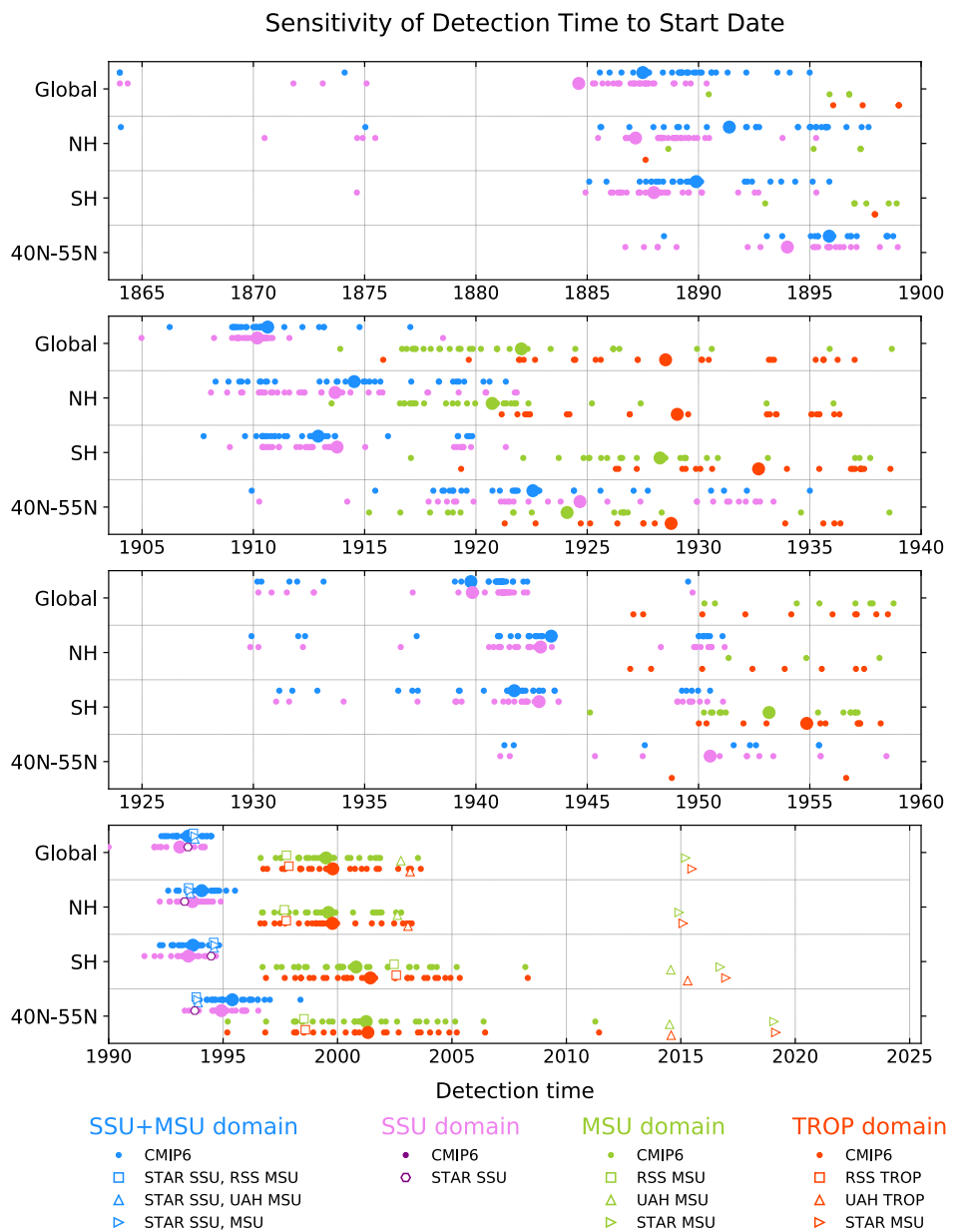


Fig. 4. Sensitivity of anthropogenic fingerprint detection time, t_d , to the selected start date for monitoring atmospheric temperature change. Values of t_d were calculated using the S/N ratios from the right-hand column of Fig. 3. The four rows provide (from top to bottom) the detection times for monitoring start dates of 1860, 1900, 1920, and 1986. For each assumed start date, values of t_d are given for the four vertical domains (SSU+MSU, SSU, MSU, and TROP), and for four geographical domains: global (90°N – 90°S), NH (0° – 90°N), SH (90°S – 0°), and NH mid-latitudes (40°N – 55°N). Fingerprint detection times in individual model HIST_{ext} realizations are indicated by smaller filled colored circles. Larger filled colored circles denote the multimodel average t_d value, which is only plotted if the fingerprint is detectable at the 1% significance level within 40 y after the 1860, 1900, and 1920 start dates (or within 39 y after the 1986 start date) in at least 10 HIST_{ext} realizations. Fingerprint detection times in satellite data are represented by unfilled color symbols.

and $T_{obs}(t)$ (*SI Appendix*, Fig. S7). The filtered $T_{hist}(t)$ time series in *SI Appendix* Fig. S8 have large intermodel differences in the stratospheric temperature response to Pinatubo. These differences bias estimates of pure natural internal variability from the HIST_{ext} runs.⁴

The effects of this bias are evident in Fig. 5, which compares σ_{FILT} , the temporal SD of the filtered $T_{ctf}(t)$, $T_{hist}(t)$, and $T_{obs}(t)$ time series. In the four stratospheric layers, σ_{FILT} values

in the CMIP6 HIST_{ext} runs are always larger than in the control runs generated with the same nine CMIP6 models. Values of σ_{FILT} in the HIST_{ext} runs are also consistently larger than in most satellite datasets. In contrast, σ_{FILT} values in most of the more than 180 samples computed from filtered control run temperatures are generally smaller than σ_{FILT} values calculated from satellite stratospheric temperature data.

As noted above, part of the reason for the latter result is that $T_{obs}(t)$ contains forced variability that is not represented in the control runs. One example is the stratospheric cooling caused by a large release of water vapor after the January 2022 Hunga Tonga eruption (29) (*SI Appendix*, Fig. S5). We reduced the impact of Hunga Tonga on model-data σ_{FILT} comparisons by excluding January 2022 to December 2024 from σ_{FILT} calculations.

⁴With adequate ensemble sizes for estimating and removing the “single model” forced signals in each of the nine models analyzed here, the effect on $T_{hist}(t)$ of large intermodel differences in the response to forcing would be strongly reduced. However, only one of the nine models which fulfilled the required criteria for calculating synthetic SSU temperatures had at least 10 ensemble members (*SI Appendix*). This is why we subtract the MMA from each of the 32 individual HIST_{ext} realizations rather than subtracting the individual model ensemble means.

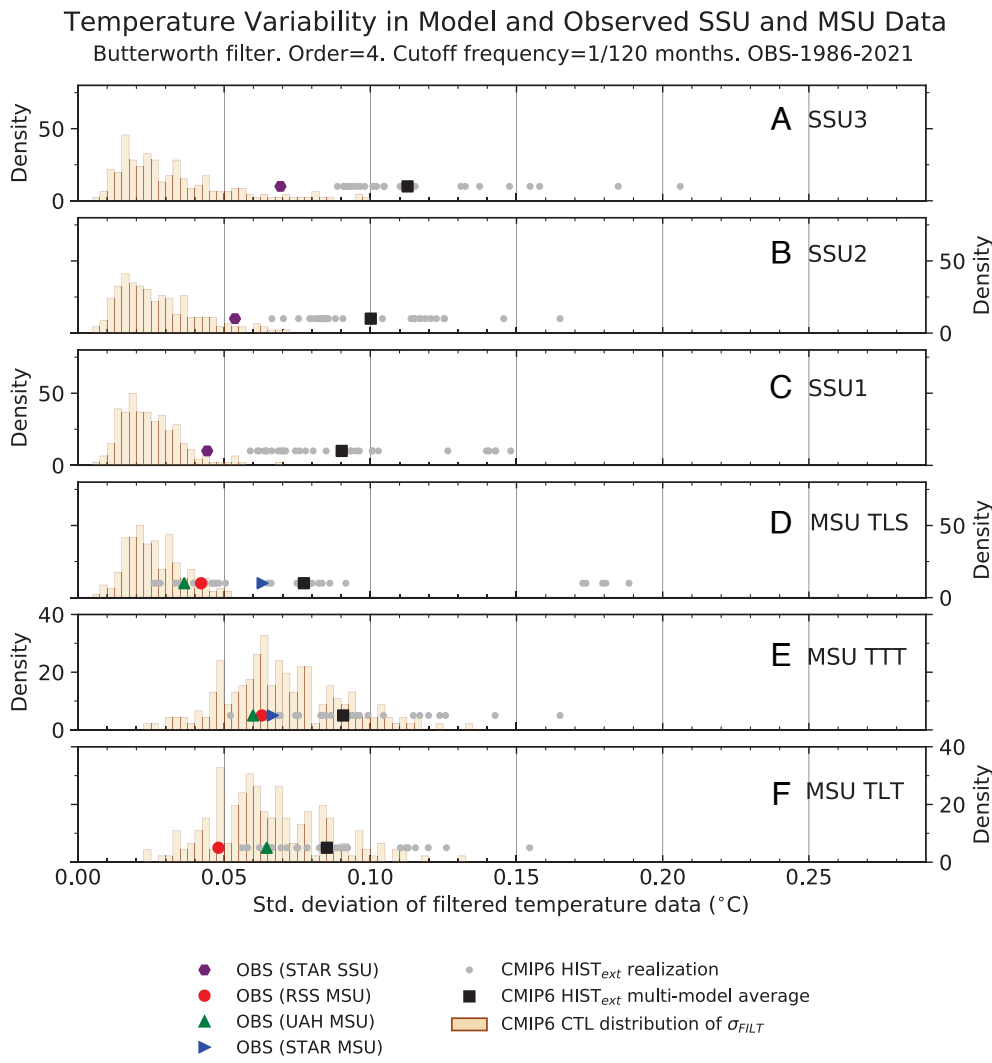


Fig. 5. Comparison of the natural internal variability of global-mean monthly-mean atmospheric temperature in six different atmospheric layers: SSU3, SSU2, SSU1, TLS, TTT, and TLT (panels A–F). Model estimates of internal variability are from two sources: preindustrial control runs (CTL) and externally forced $HIST_{ext}$ simulations from which the multimodel average temperature time series (MMA) was subtracted. A regression-based approach was used to remove the MMA from observed temperature time series (54). Temperatures from the CTL simulations and the “MMA-removed” $HIST_{ext}$ realizations and satellite temperature data were digitally smoothed to compare variability on timescales of approximately 10 y (*SI Appendix*). The statistic plotted is σ_{FILT} , the temporal SD of the filtered data. All $HIST_{ext}$ and observed time series were linearly detrended after removal of the MMA. The 432-mo analysis period in the $HIST_{ext}$ realizations and satellite data (January 1986 to December 2021) excludes the January 2022 Hunga Tonga eruption, which is not included in the $HIST_{ext}$ simulations but had a large effect on observed stratospheric temperature (*SI Appendix*, Fig. S6). The CTL run distributions of σ_{FILT} are based on analysis of over 180 nonoverlapping 432-mo segments of $T_{ctl}(t)$ data.

Model-data σ_{FILT} comparisons are still affected, however, by other missing or incorrectly specified forcings. One example is the mismatch between the assumed solar forcing after the end of the historical runs in December 2014 (26) and the actual post-2014 solar forcing that occurred in the real world. This and other forcing mismatches inflate the observed residual variance and contribute to larger σ_{FILT} values in satellite stratospheric temperatures than in model control run data. We cannot exclude the possibility that a low bias in control run σ_{FILT} values may also be partly due to a systematic model underestimate of observed decadal-timescale stratospheric temperature variability.

It is unlikely that such a model variability bias could significantly affect the detection times in Fig. 4. We demonstrate this by calculating $R1$, the ratio between the observed linear trends in stratospheric temperature over 1986–2021 and the mean of the control run distribution of σ_{FILT} . In the three SSU channels, $R1$ always exceeds 60. Values of $R1$ for the lower stratosphere vary from 21 to 29, depending on the choice of observed TLS

dataset. Model estimates of the observed pure internal variability would therefore need to be biased low by an order of magnitude for decadal-timescale intrinsic variability to fully explain the large observed stratospheric cooling trends. There is no evidence from Fig. 5 that an error of this magnitude exists. If the observed σ_{FILT} results in Fig. 5 are used to estimate the denominator of $R1$, the $R1$ values remain well beyond the five sigma standard for particle discovery in physics,[#] ranging from 31 to 38 for the three SSU channels and from 9 to 21 for TLS.

The σ_{FILT} values for global-mean temperature in the unforced control runs are larger in the troposphere than in the stratosphere (Fig. 5).[¶] This helps to explain why the signatures of model forcing/response errors and missing forcings are clearer in the

[#]<https://home.cern/resources/faqs/five-sigma>.

[¶]This is primarily due to global averaging. Global averaging effectively averages out most of the dynamic variability that leads to locally large temperature variability in the stratosphere.

stratosphere than in the troposphere. The key tropospheric σ_{FILT} result is that for both TTT and TLT, CMIP6 models do not systematically underestimate the amplitude of the observed intrinsic variability on 10-y timescales (53, 54). In contrast to the variability comparison in the stratosphere, the satellite-derived σ_{FILT} results for TTT and TLT are well within the control run sampling distributions of σ_{FILT} .

Conclusions

When could scientists have first known that human activities were altering Earth's climate? We addressed this question here by performing a simple thought experiment. We assumed that the capability to measure global temperature changes in the mid- to upper stratosphere, with today's measurement accuracy and geographical coverage, existed in 1860. If scientists had commenced monitoring atmospheric temperature at that time, only 25 y would have been required to identify the stratospheric cooling signal arising from human-caused fossil fuel burning and relatively small CO₂ increases (*SI Appendix*, Fig. S1). Put differently, a human fingerprint on stratospheric temperature could have been identified with high confidence as early as 1885—over 130 y ago.

Even if our monitoring capability in 1860 had not been global, and high-quality stratospheric temperature measurements existed for Northern Hemisphere mid-latitudes only, it still would have been feasible to detect human-caused stratospheric cooling by 1894, only 34 y after the assumed start of climate monitoring. The latter result is partly due to the fact that the NH mid-latitudes exclude the large stratospheric temperature variability of the Arctic, but still sample pronounced anthropogenic stratospheric cooling.

Early detection of human effects on stratospheric temperature occurs because the mid- to upper stratosphere is an environment where human-caused stratospheric cooling is large (15, 33, 39) and the patterns of signal and noise are spatially different. In the troposphere, however, global-mean anthropogenic signals are smaller and signal and noise patterns are more similar (18). Robust anthropogenic fingerprint identification in the troposphere would not have been feasible for an 1860 climate monitoring start date and 40 y of continuous temperature measurements. It is only for assumed monitoring start dates on or after 1960 that we obtain consistent detection of anthropogenic fingerprints in tropospheric temperature (Fig. 4 and *SI Appendix*, Fig. S4).

In both the stratosphere and the troposphere, fingerprint detection time is influenced by the interplay between anthropogenic signal strength, the natural external forcing arising from solar variability and volcanic activity (23, 24), and the stipulated significance level for fingerprint identification. In the mid- to upper stratosphere, for example, temperature variability driven by the 11-y cycle of solar irradiance fluctuations can temporarily affect the detection of human-caused stratospheric cooling, particularly for early monitoring start dates sampling relatively small anthropogenic signals (Figs. 1 and 3). Low-frequency changes in the amplitude of the 11-y solar cycle (26) can also influence stratospheric signal detection. Because of such low-frequency changes, the time required for anthropogenic signal detection does not decrease monotonically for later assumed monitoring start dates, even as CO₂-driven cooling of the mid- to upper stratospheric increases over time (Figs. 1 and 4). Large volcanic eruptions can also temporarily delay anthropogenic signal detection, both in the stratosphere and the troposphere,

and have longer-lasting effects on tropospheric temperature signals due to the large thermal inertia of the ocean (43, 58).

Such simple thought experiments are useful tools for learning about anthropogenic signal detection in the real world. Similar thought experiments can be performed for other climate variables, such as changes in ocean heat content or in sea level. In the latter case, long-term tide gauge measurements could be employed to determine whether model-based estimates of signal detection time are in accord with observations (59). For the example considered here, it would be useful to explore whether suitable long-term atmospheric temperature records from radiosondes (9–11, 60), airglow measurements (61), lidar, and rocketsondes allow cross-checking of model-inferred signal detection times against detection times inferred from early observations.

Our study reveals that with suitable high-quality temperature measurements, a “discernible human influence on global climate” (62) could have been detected by the end of the 19th century. It is unclear whether such early knowledge of the climate-altering consequences of fossil fuel burning would have prompted human societies to follow a more environmentally sustainable greenhouse gas emissions pathway. Today, however, we know with high confidence that sustainable pathways must be followed to avoid dangerous anthropogenic interference with climate. For the mid- to upper stratosphere and the troposphere, the projected future changes over the next 26 y are larger than the simulated changes over the 39-y period from 1986 to 2024 (*SI Appendix*, Fig. S10). Humanity is now at the threshold of dangerous anthropogenic interference. Our near-term choices will determine whether or not we cross that threshold.

Materials and Methods

Satellite Data. We rely on satellite data from three groups: Remote Sensing Systems (RSS) (63), the Center for Satellite Applications and Research (STAR) (64, 65), and the University of Alabama at Huntsville (UAH) (31). STAR is the only current source of spatially resolved temperature data for SSU channels 1, 2, and 3 (21). STAR, RSS, and UAH each supply MSU-based measurements of the temperatures of the lower stratosphere (TLS), the mid- to upper troposphere (TMT), and the lower troposphere (TLT). We apply a standard regression-based method to adjust TMT for the influence it receives from lower stratospheric cooling (66, 67), thereby obtaining the temperature of the total troposphere (TTT). See *SI Appendix* for details.

Model Data. The model synthetic SSU and MSU temperatures analyzed here are from phase 6 of CMIP6 (32). “Synthetic” indicates that the model results were calculated with appropriate weighting functions (33), thus facilitating direct comparison between satellite and model temperature changes (*SI Appendix*).

The synthetic SSU and MSU temperatures are from three different types of numerical experiment: 1) simulations with estimated historical changes in natural and anthropogenic external forcings, which typically commence in January 1850 and end in December 2014; 2) scenario runs with post-2014 changes in anthropogenic external forcings that are specified according to a Shared Socioeconomic Pathway which reaches radiative forcing of 8.5 W/m² by 2100 (SSP5-8.5); and 3) preindustrial control integrations with no year-to-year changes in external forcings.

The CMIP6 historical and scenario simulations consider not only the effects of CO₂ increases but also include the radiative effects of changes in other greenhouse gases (68), anthropogenic aerosols, and solar and volcanic forcing. Temperatures from historical simulations and corresponding scenario runs were spliced together to permit comparison of model and observational results over 1986 to 2024. We refer to these as extended historical runs (HIST_{ext}; *SI Appendix*). The CMIP6 model historical and SSP5-8.5 simulations used in our study are identified in *SI Appendix, Table S1*. The control runs required for noise estimation are listed in *SI Appendix, Table S2*. We analyzed a total of 32 HIST_{ext} realizations

performed with nine different models and control runs generated with the same nine models.

Fingerprint and Signal Trends. We project zonal-mean annual-mean atmospheric temperature onto a searched-for fingerprint pattern, $F(x, p)$, estimated from the multimodel average temperature changes in the HIST_{ext} simulations. This yields the projection time series $Z(t)$, a measure of uncentered spatial covariance (SI Appendix). The indices x , p , and t are over latitude, atmospheric layer, and time (respectively). The $T(x, p, t)$ temperature data projected onto $F(x, p)$ are either from satellite observations or individual HIST_{ext} realizations. $Z(t)$ is a measure of the evolving pattern similarity between $F(x, p)$ and $T(x, p, t)$ at each year t . We compute L -year least-squares linear trends in $Z(t)$, starting in 1860, 1900, 1920, and 1986 in Fig. 3. The latter start date is the beginning of continuous SSU records. In SI Appendix, Fig. S3, we also consider four additional start dates: 1940, 1950, 1960, and 1970. For each start date, the first trend length L is 5 y. We increase L in 1-y increments, with a maximum value of $L = 40$ y for each start date, except for 1986, for which the maximum L value is only 39 y (the current length of complete SSU temperature records over 1986 to 2024). For an assumed 1860 start date, $L = 5$ and $L = 40$ correspond to the analysis periods 1860 to 1864 and 1860 to 1899, respectively. The signal $S(L)$ is the L -year least-squares trend in $Z(t)$. Large $S(L)$ trends denote time-increasing similarity between the latitude-height temperature changes in $T(x, p, t)$ and the fingerprint pattern.

Noise Trends. To determine whether and when the values of $S(L)$ in Fig. 3 A, C, E, and G achieve statistical significance, we compare $S(L)$ with null distributions in which we know a priori that natural internal variability is the only explanation for trends in pattern similarity. We use control runs with no year-to-year changes in external forcing to generate these “no signal” distributions. We project a total of 4,050 y of atmospheric temperature data from nine CMIP6 preindustrial control runs onto the SSU+MSU SSU, MSU, and TROP fingerprints, resulting in a projection time series $N_{ctf}(t)$ for each fingerprint. Nonoverlapping L -year trends in $N_{ctf}(t)$ are then calculated for each value of L considered (i.e., for $L = 5, 6, \dots, 40$ y). For the $L = 40$ -y analysis period, there are 101 individual samples of trends in $N_{ctf}(t)$. The SD of these L -year noise trend distributions, $\sigma_{ctf}(L)$, is the denominator of the S/N ratios in Fig. 3 B, D, F, and H.

Digital Filtering. We compare modeled and observed temperature variability on the 10-y timescale by applying a fourth-order Butterworth filter with a 1/120 mo cutoff frequency (SI Appendix, Fig. S7) to the global-mean monthly mean $T_{ctf}(t)$ data and to the “signal removed” $T_{obs}(t)$ and $T_{hist}(t)$ time series. To avoid phase-shifting of the filtered data, we use the `scipy` “`filtfilt`” routine, which applies the Butterworth filter twice (forward and backward; <https://docs.scipy.org/doc/scipy/reference/generated/scipy.signal.filtfilt.html>). Treatment of

the signal edges relies on the default “`filtfilt`” options. Alternative choices of filter type, order, cutoff frequency, and treatment of signal edges do not alter the primary conclusions of this paper.

The statistic plotted in Fig. 5 and in SI Appendix, Fig. S9 is σ_{FILT} , the temporal SD of the digitally filtered $T_{ctf}(t)$, $T_{obs}(t)$, and $T_{hist}(t)$ time series. In the satellite data and HIST_{ext} runs, σ_{FILT} is calculated over the 432-mo period January 1986 to December 2021 to exclude the Hunga Tonga eruption, which influenced observed atmospheric temperature but was not included in the HIST_{ext} runs.

Data, Materials, and Software Availability. Analysis codes, observational satellite temperature data (MSU, AMSU, and SSU) and synthetic satellite temperature data from CMIP6 simulation output have been deposited in Zenodo (<https://doi.org/10.5281/zenodo.15103284>) (69).

ACKNOWLEDGMENTS. We acknowledge the World Climate Research Programme’s Working Group on Coupled Modelling, which is responsible for CMIP, and we thank the climate modeling groups for producing and making available their model output. For the Coupled Model Intercomparison Project (CMIP), the U.S. Department of Energy’s Program for Climate Model Diagnosis and Intercomparison (PCMDI) provides coordinating support and led development of software infrastructure in partnership with the Global Organization for Earth System Science Portals. B.D.S. was supported by the Francis E. Fowler IV Center for Ocean and Climate at Woods Hole Oceanographic Institution (WHOI). S.S. gratefully acknowledges support as the Martin Professor in Environmental Studies at M.I.T. D.W.J.T. was supported by NASA under 80NSSC23K0113 and the NSF Climate and Large-Scale Dynamics Program under AGS-2116186. Q.F. was partly supported by the NSF Grant AGS-2202812 and the Calvin Professorship in Atmospheric Sciences. Y.L. gratefully acknowledges support from the NOAA Climate & Global Change Postdoctoral Fellowship Program under NOAA Science Collaboration Program Award NA23OAR4310383B. Ray Shi (WHOI) and Thomas Birner (Ludwig-Maximilians University Munich, Germany) provided helpful comments on the paper. Paul Durack and Steve Po-Chedley (PCMDI) provided assistance with retrieval and plotting of the CO₂ data in SI Appendix, Fig. S1.

Author affiliations: ^aPhysical Oceanography Department, Woods Hole Oceanographic Institution, Woods Hole, MA 02543; ^bJoint Institute for Regional Earth System Science and Engineering, University of California at Los Angeles, Los Angeles, CA 90095; ^cEarth, Atmospheric, and Planetary Sciences, Massachusetts Institute of Technology, Cambridge, MA 02139; ^dDepartment of Atmospheric Sciences, Colorado State University, Fort Collins, CO 80521; ^eSchool of Environmental Sciences, University of East Anglia, Norwich NR4 7TJ, United Kingdom; and ^fDepartment of Atmospheric Sciences, University of Washington, Seattle, WA 98195

1. R. Jackson, Eunice Foote, John Tyndall and a question of priority. *Notes Rec.* **74**, 105–118 (2020).
2. E. Crawford, Arrhenius’ 1896 model of the greenhouse effect in context. *AMBI/O* **26**, 6–11 (1997).
3. S. Arrhenius, *Das Werden Der Welten* (Academic Publishing House, Leipzig, Germany, 1908), p. 208.
4. P. D. Jones, The climate of the past 1000 years. *Endeavor* **14**, 129–136 (1990).
5. K. Hoinka, The tropopause: Discovery, definition, demarcation. *Meteorol. Z.* **6**, 281–303 (1997).
6. L. T. de Bort, Variations de la température de l’air libre dans la zone comprise entre 8 km et 13 km d’altitude. *C. R. Séances Acad. Sci. Paris* **134**, 987–989 (1902).
7. D. Shaw, Leon Philippe Teisserenc de Bort. *Nature* **90**, 519–520 (1913).
8. R. Assmann, Über die Existenz eines wärmeren Luftstromes in der Höhe von 10 bis 15 km. *Sitzungsber. Königlich-Preußischen Akad. Wiss. Berlin* **24**, 495–504 (1902).
9. P. W. Thorne *et al.*, Revisiting radiosonde upper air temperatures from 1958 to 2002. *J. Geophys. Res.* **110**, D18105 (2005).
10. I. Durre, R. S. Vose, D. B. Wuertz, Overview of the integrated global radiosonde archive. *J. Clim.* **19**, 53–68 (2006).
11. S. Brönnimann, T. Giessler, A. Stickler, A gridded monthly upper-air data set from 1918 to 1957. *Clin. Dyn.* **38**, 475–493 (2012).
12. D. Etheridge *et al.*, Natural and anthropogenic changes in atmospheric CO₂ over the last 1000 years from air in Antarctic ice and FIRN. *J. Geophys. Res.* **101**, 4115–4128 (2014).
13. C. M. Meure *et al.*, Law Dome CO₂, CH₄ and N₂O ice core records extended to 2000 years BP. *Geophys. Res. Lett.* **33**, L14810 (2006).
14. W. F. Ruddiman, F. He, S. J. Vavrus, J. Kutzbach, The early anthropogenic hypothesis: A review. *Q. Sci. Rev.* **240**, 106386 (2020).
15. S. Manabe, R. T. Wetherald, Thermal equilibrium of the atmosphere with a given distribution of relative humidity. *J. Atmos. Sci.* **24**, 241–259 (1967).
16. N. Abram *et al.*, Early onset of industrial-era warming across the oceans and continents. *Nature* **536**, 411–418 (2016).
17. J. Duan *et al.*, Detection of human influences on temperature seasonality from the 19th century. *Nat. Sustainability* **2**, 484–490 (2019).
18. B. D. Santer *et al.*, Exceptional stratospheric contribution to human fingerprints on atmospheric temperature. *Proc. Natl. Acad. Sci. U.S.A.* **120**, e2300758120 (2023).
19. M. Meinshausen *et al.*, Historical greenhouse gas concentrations for climate modelling (CMIP6). *Geosci. Mod. Dev.* **10**, 2057–2116 (2017).
20. D. G. Andrews, J. R. Holton, C. B. Leovy, *Middle Atmosphere Dynamics* (Academic Press, London, UK, 1987), p. 489.
21. C. Z. Zou, H. Qian, Stratospheric temperature climate record from merged SSU and AMSU-A observations. *J. Atmos. Ocean. Tech.* **33**, 1967–1984 (2016).
22. C. Mears, F. J. Wentz, Sensitivity of satellite-derived tropospheric temperature trends to the diurnal cycle adjustment. *J. Clim.* **29**, 3629–3646 (2016).
23. G. C. Hegerl, S. Brönnimann, A. Schurer, T. Cowan, The early 20th century warming: Anomalies, causes, and consequences. *WIREs Clim. Change* **9**, e522 (2018).
24. G. C. Hegerl *et al.*, Causes of climate change over the historical record. *Environ. Res. Lett.* **14**, 123006 (2019).
25. A. Robock, Volcanic eruptions and climate. *Rev. Geophys.* **38**, 191–219 (2000).
26. K. Matthes *et al.*, Solar forcing for CMIP6 (v3.2). *Geosci. Model. Dev.* **10**, 2247–2302 (2017).
27. D. W. J. Thompson *et al.*, The mystery of recent stratospheric temperature trends. *Nature* **491**, 692–697 (2012).
28. T. R. Karl, S. J. Hassol, C. D. Miller, W. L. Murray, Eds., *Temperature Trends in the Lower Atmosphere: Steps for Understanding and Reconciling Differences. A Report by the U.S. Climate Change Science Program and the Subcommittee on Global Change Research* (National Oceanic and Atmospheric Administration, Washington DC, 2006), p. 164.
29. W. J. Randel, X. Wang, J. Starr, R. R. Garcia, D. E. Kinnison, Long-term temperature impacts of the Hunga volcanic eruption in the stratosphere and above. *Geophys. Res. Lett.* **51**, e2024GL111500 (2024).

30. S. Solomon *et al.*, The persistently variable "background" stratospheric aerosol layer and global climate change. *Science* **333**, 866–870 (2011).
31. R. W. Spencer, J. R. Christy, W. D. Braswell, UAH version 6 global satellite temperature products: Methodology and results. *Asia-Pac. J. Atmos. Sci.* **53**, 121–130 (2017).
32. V. Eyring *et al.*, Overview of the coupled model intercomparison project phase 6 (CMIP6) experimental design and organization. *Geosci. Mod. Dev.* **9**, 1937–1958 (2016).
33. A. Steiner *et al.*, Observed temperature changes in the troposphere and stratosphere from 1979 to 2018. *J. Clim.* **33**, 8165–8194 (2020).
34. S. B. Fels, J. D. Mahlman, M. D. Schwarzkopf, R. W. Sinclair, Stratospheric sensitivity to perturbations in ozone and carbon dioxide: Radiative and dynamical response. *J. Atmos. Sci.* **37**, 2265–2297 (1980).
35. S. Solomon, Stratospheric ozone depletion: A review of concepts and history. *Rev. Geophys.* **37**, 275–316 (1999).
36. V. Ramaswamy, M. D. Schwarzkopf, Effects of ozone and well-mixed gases on annual-mean stratospheric temperature trends. *Geophys. Res. Lett.* **29**, 21.1–21.4 (2002).
37. K. P. Shine *et al.*, A comparison of model-simulated trends in stratospheric temperatures. *Q. J. Roy. Met. Soc.* **129**, 1565–1588 (2003).
38. V. Ramaswamy *et al.*, Anthropogenic and natural influences in the evolution of lower stratospheric cooling. *Science* **311**, 1138–1141 (2006).
39. H. F. Goessling, S. Bathiany, Why CO₂ cools the middle atmosphere—A consolidating model perspective. *Earth Syst. Dyn.* **7**, 697–715 (2016).
40. A. C. Maycock *et al.*, Revisiting the mystery of recent stratospheric temperature trends. *Geophys. Res. Lett.* **45**, 9919–9933 (2018).
41. M. C. Casas *et al.*, Understanding model-observation discrepancies in satellite retrievals of atmospheric temperature using GISS ModelE. *J. Geophys. Res.* **128**, e2022JD037523 (2022).
42. C. Bonfils *et al.*, Human influence on joint changes in temperature, rainfall and continental aridity. *Nat. Clim. Change* **10**, 726–731 (2020).
43. D. W. J. Thompson, J. M. Wallace, P. D. Jones, J. J. Kennedy, Identifying signatures of natural climate variability in time series of global-mean surface temperature: Methodology and insights. *J. Clim.* **22**, 6120–6141 (2009).
44. B. D. Santer *et al.*, Quantifying stochastic uncertainty in detection time of human-caused climate signals. *Proc. Nat. Acad. Sci. U.S.A.* **116**, 19821–19827 (2019).
45. K. Hasselmann, *On the Signal-to-Noise Problem in Atmospheric Response Studies* (Royal Meteorological Society, London, UK, 1979), pp. 251–259.
46. G. C. Hegerl *et al.*, Detecting anthropogenic climate change with an optimal fingerprint method. *J. Clim.* **9**, 2281–2306 (1996).
47. S. F. B. Tett, J. F. B. Mitchell, D. E. Parker, M. R. Allen, Human influence on the atmospheric vertical temperature structure: Detection and observations. *Science* **274**, 1170–1173 (1996).
48. M. R. Allen, S. F. B. Tett, Checking for model consistency in optimal fingerprinting. *Clin. Dyn.* **15**, 419–434 (1999).
49. P. A. Stott *et al.*, External control of 20th century temperature by natural and anthropogenic forcings. *Science* **290**, 2133–2137 (2000).
50. N. P. Gillett, F. W. Zwiers, A. J. Weaver, P. A. Stott, Detection of human influence on sea-level pressure. *Nature* **422**, 292–294 (2003).
51. B. D. Santer *et al.*, A search for human influences on the thermal structure of the atmosphere. *Nature* **382**, 39–46 (1996).
52. R. J. Stouffer, S. Manabe, Assessing temperature pattern projections made in 1989. *Nat. Clim. Change* **7**, 163–165 (2017).
53. J. Pallotta, B. D. Santer, Multi-frequency analysis of simulated versus observed variability in tropospheric temperature. *J. Clim.* **33**, 10383–10402 (2020).
54. B. D. Santer *et al.*, Robust anthropogenic signal identified in the seasonal cycle of tropospheric temperature. *J. Clim.* **35**, 6075–6100 (2022).
55. N. P. Gillett, M. R. Allen, S. F. B. Tett, Modelled and observed variability in atmospheric vertical temperature structure. *Clim. Dyn.* **16**, 49–61 (2000).
56. L. M. Frankcombe, M. H. England, M. E. Mann, B. A. Steinman, Separating internal variability from the externally forced climate response. *J. Clim.* **28**, 8184–8202 (2015).
57. B. A. Steinman, M. E. Mann, S. K. Miller, Atlantic and Pacific multidecadal oscillations and Northern Hemisphere temperatures. *Science* **347**, 988–991 (2015).
58. B. D. Santer *et al.*, Celebrating the anniversary of three key events in climate change science. *Nat. Clim. Change* **9**, 180–182 (2019).
59. J. S. Walker, R. E. Kopp, C. M. Little, B. P. Horton, Timing of emergence of modern rates of sea-level rise by 1863. *Nat. Commun.* **13**, 966 (2022).
60. V. Ramaswamy *et al.*, Stratospheric temperature trends: Observations and model simulations. *Rev. Geophys.* **39**, 71–122 (2001).
61. T. Y. Huang, M. Vanyo, Trends in the airglow temperatures in the MLT region—Part 1: Model simulations. *Atmosphere* **11**, 468 (2020).
62. B. D. Santer, T. M. L. Wigley, T. P. Barnett, E. Anyamba, "Detection of climate change and attribution of "causes" in "Climate" Change 1995: The Science of Climate Change" in *Contribution of Working Group I to the Second Assessment Report of the Intergovernmental Panel on Climate Change*, J. T. Houghton *et al.*, Eds. (Cambridge University Press, New York, NY, 1995), pp. 407–443.
63. C. Mears, F. J. Wentz, A satellite-derived lower-tropospheric atmospheric temperature dataset using an optimized adjustment for diurnal effects. *J. Clim.* **30**, 7695–7718 (2017).
64. C. Z. Zou, M. D. Goldberg, X. Hao, New generation of U.S. satellite microwave sounder achieves high radiometric stability performance for reliable climate change detection. *Sci. Adv.* **4**, eaau0049 (2018).
65. C. Z. Zou, H. Xu, X. Hao, Q. Liu, Mid-tropospheric layer temperature record derived from satellite microwave sounder observations with backward merging approach. *J. Geophys. Res.* **128**, e2022JD037472 (2023).
66. Q. Fu, C. M. Johanson, S. G. Warren, D. J. Seidel, Contribution of stratospheric cooling to satellite-inferred tropospheric temperature trends. *Nature* **429**, 55–58 (2004).
67. Q. Fu, C. M. Johanson, Stratospheric influences on MSU-derived tropospheric temperature trends: A direct error analysis. *J. Clim.* **17**, 4636–4640 (2004).
68. B. Govindasamy *et al.*, Limitations of the equivalent CO₂ approximation in climate change simulations. *J. Geophys. Res.* **106**, 22593–22603 (2001).
69. B. D. Santer, Model simulation output, satellite data, and analysis codes for 2025 Santer *et al.* PNAS paper. Zenodo. <https://zenodo.org/records/15103284>. Deposited 28 March 2025.